Post-Print

This is the accepted version of:

Z.F. Luo, F. Topputo
Mars Orbit Insertion via Ballistic Capture and Aerobraking
Astrodynamics, In press - Published online 07/01/2021
doi:10.1007/s42064-020-0095-4

Mars Orbit Insertion via Ballistic Capture and Aerobraking

Zong-Fu Luo[a,*], Francesco Topputo[b]

[a] *School of Astronomy and Space Science, Nanjing University, Nanjing 210023, P. R. China*
[b] *Department of Aerospace Science and Technology, Politecnico di Milano, Via La Masa, 34, 20156, Milano, Italy*

Abstract

A novel Mars orbit insertion strategy that combines ballistic capture and aerobraking is presented. Mars ballistic capture orbits that neglect aerodynamics are first generated, which are distilled from properly computed stable and unstable sets by using an already-established method. A small periapsis maneuver is implemented at first close encounter to better submit the post-capture orbit to the aerobraking process. An ad-hoc patching point marks the transition from ballistic capture to aerobraking, from which an exponential model simulating Mars atmosphere and a box-wing satellite configuration is considered. A series of apoapsis trim maneuvers are then computed by targeting a prescribed pericenter dynamic pressure. The aerobraking duration is estimated by using a simplified two-body model. A yaw angle tuning cancels inclination deflections due to out-of-plane perturbation from the Sun. A philosophy combining in-plane and out-of-plane dynamics is proposed to achieve the required semi-major axis and inclination simultaneously. Numerical simulations indicate that the developed method is more efficient in terms of fuel consumption, insertion safety, and flexibility than state-of-the-art insertion strategies.

Keywords: Ballistic capture, Aerobraking, Mars orbit insertion

1. Introduction

Patched conics approximation is widely used in astrodynamics as it decomposes an involute route into a succession of simpler Keplerian orbit pieces. Common Earth–Mars transfers are constructed by application of the patched conics method; the goal is to minimize the launch mass, or equivalently, to maximize the mass of the

*Corresponding author.
Email addresses: luozf@nju.edu.cn (Zong-Fu Luo), francesco.topputo@polimi.it (Francesco Topputo)

payload delivered. In these cases, a chemical burn is used to inject the spacecraft into a low-altitude, near-circular orbit around Mars. This process, or Mars orbit insertion (MOI), involves maneuvering at the periapsis of the incoming hyperbola [1, 2]. Overall, this approach facilitates the preliminary trajectory designs, yet it has drawbacks: 1) A considerable amount of propellant is used to cancel the hyperbolic excess velocity upon arrival; 2) The periapsis insertion maneuver exposes the mission to a high risk of failure if the retro-engine is off-nominal [3]; 3) The launch window are mainly dictated by the relative geometry between the Earth and Mars, and this engenders a fixed two-year launch period from the Earth [1].

Another option consists of using aerobraking. Following the incoming hyperbola, a moderate periapsis burn is used to deploy the spacecraft into an elongated elliptic orbit, so exposing it to multiple atmospheric passages across the periapsis. The orbit is gradually circularized because of the energy dissipation in the atmospheric phases [4, 5]. This mechanism reduces significantly the Δv to acquire the final orbit, so making it attractive for Mars missions [6]. In the Mars Global Surveyor (MGS) mission, at least 1 km/s was saved using aerobraking [2, 7]. Moreover, the data gathered by on-board sensors may be used to estimate aerodynamic and atmospheric parameters [8, 9]. Aerobraking was demonstrated by Hiten [10], and was applied in Venusian missions Magellan [11] and Venus Express [12], and Martian missions MGS [7], Odysssey [13] and Mars Reconnaissance Orbiter (MRO) [14]. It has also been proposed in ExoMars [15].

Mars ballistic capture has recently emerged as a valid alternative to patched conics [3]. A proper use of attractions from the Sun and Mars allows a spacecraft to approach Mars and enter a temporarily captured orbit without requiring maneuvers in between. Ballistic capture may reduce fuel expenditure at the price of a longer Mars approach time [16, 17]. It also provides multiple MOI opportunities, so mitigating the risks associated to a single-point burn [18, 19, 20]. From an operational point of view, this benign process is safer than performing a high or moderate capture maneuver, as required by a Hohmann transfer or a conventional aerobraking. Stabilization maneuvers can even be totally canceled if temporary, irregular capture orbits are tolerated [21, 22, 23, 24, 25]. Moreover, ballistic capture can provide more flexible launch opportunities because the paradigm is no longer to target a physical point in space, but rather reaching a manifold that supports capture [3, 26]. Ballistic capture has been successfully employed in lunar transfers [27, 28, 29, 30] and baselined for the exploration of Mercury [31, 32].

Although both aerobraking and ballistic capture economize on fuel consumption over patched conics, they are not immune by deficiencies. A moderate Δv is still required before delivering the spacecraft into a low Mars orbit for both alternatives:

1) Ballistic capture offers, at most, 25% fuel savings over a Hohmann transfer to Mars [3]; 2) A ∼1 km/s maneuver was needed to insert MGS into a $54,025.9 \times 262.9$ km elliptical orbit [2]. Moreover, aerobraking is subject to single-point failures and similar launch windows constraints as patched conics. In addition, both methods extend considerably the time to acquire the final orbit.

This paper revisits ballistic capture and aerobraking to find a compromise for their use in Mars missions. A judicious integration involving multi-body dynamics, aerodynamics, and aerothermodynamics is devised. Mars approaching orbits that support ballistic capture are first generated using the stable sets method [20, 33]. A small periapsis maneuver is performed at the first close passage. A patching point is used to switch to a simulation of the aerobraking process. The atmospheric phase features periapsis trim maneuvers and yaw angle tuning to target a prescribed dynamic pressure and inclination, respectively. Simulations provide quantitative results.

The remainder of the manuscript is organized as follows. Section 2 summarizes background information. Section 3 presents the method developed to merge ballistic capture and aerobraking. Numerical results are reported in Section 4. Some underling conclusions are drawn in Section 5. Supplementary material is provided in the Appendix.

2. Background

We study the motion of an unmanned spacecraft approaching Mars, subject to the gravitational attractions of the Sun and Mars, as well as to the aerodynamic force exerted by the atmospheric drag. The Sun and Mars are assumed to be point masses, and Mars is assumed to revolve around the Sun in an elliptic orbit. The physical constants of the model are given in Table 1, where Gm_s and Gm_p are the gravitational parameters of the Sun and Mars, respectively. For the latter: R is the mean equatorial radius, Ω_p is the spin angular velocity, and R_{SOI} is the radius of the sphere of influence (SOI). In our simulation $R_{\mathrm{SOI}} = a_s\,(m_p/m_s)^{2/5}$, where a_s is the semi-major axis of Mars orbiting the Sun, while m_p and m_s are their respective masses [1].

Martian atmospheric density is computed by an exponential model

$$\rho(h) = \rho_0 \exp\left[-\frac{h-h_0}{H}\right], \tag{1}$$

[1] https://nssdc.gsfc.nasa.gov/planetary/factsheet/marsfact.html

Table 1: Physical parameters of the Sun and Mars[1].

Gm_s (km^3/s^2)	Gm_p (km^3/s^2)	R (km)	Ω_p (rad/s)	R_{SOI} ($\times R$)	ρ_0 (kg/m^3)	h_0 (km)	H (km)
1.3271×10^{11}	4.2828×10^{4}	3,394.2	7.0882×10^{-5}	170.0	2.0×10^{-8}	110.0	10.0

where ρ_0 is the density at the reference height h_0 and H is the scale height; see Table 1 [2, 9].

A spacecraft similar to MGS [7], with a "box-wing" configuration comprising a box-like main body and two solar panels is considered, as shown in Fig. 1. Two solar panels are assumed to maintain a symmetric aerodynamic configuration with a 90 degree sweep angle to their normal vector $\boldsymbol{n}$ (see Fig. 1(b)).

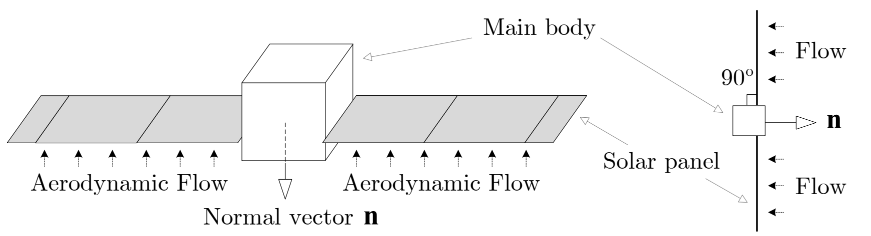

(a) Three-dimension view (b) Side view (not to scale)

Figure 1: Spacecraft aerobraking configuration.

2.1. Reference Frames

To ease the orbital analysis, a body mean equator frame at epoch t_0, (x_b, y_b, z_b), BME@t_0 for brevity, is defined (see Fig. 2). This frame is centred at Mars; its z_b-axis is aligned with the spin axis at t_0, the x_b-axis points to the ascending node of Mars mean equator at t_0 with respect to the Earth mean equator and equinox at J2000.0, and the y_b-axis completes the dextral orthonormal triad; refer to Archinal and et al. [34] for details.

A velocity-co-normal-normal frame (x_v, y_v, z_v), VCN for brevity, centred at the spacecraft, is used to decompose the aerodynamic forces. The z_v-axis is perpendicular to the orbital plane, the x_v-axis follows the spacecraft inertial velocity $\boldsymbol{v}$, and the y_v-axis completes the right-hand rule (see Fig. 2). The transformation from VCN to BME@t_0 at time t is denoted by $\mathcal{Q}_{v\to b}(t)$; it is obtained by projecting the unit vectors along velocity, orbit normal, and their cross product [1].

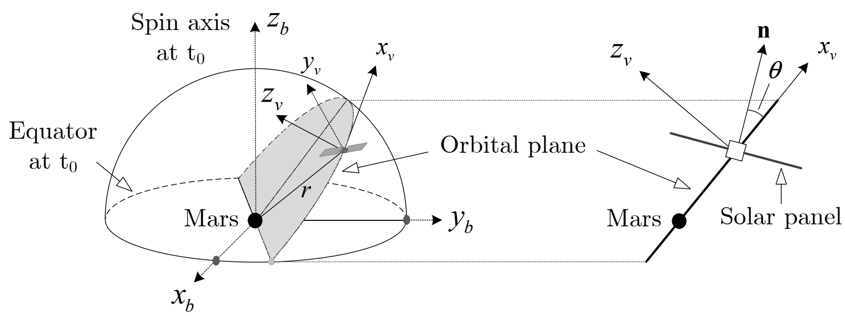

Figure 2: Geometry of reference frames.

2.2. Equations of Motion

The rotation of Martian atmosphere is not considered since the difference between the inertial velocity and airspeed of the spacecraft is small enough to be ignored. This paper only considers the case in which θ represents a rotation of $\boldsymbol{n}$ around the y_v-axis; a counter-clockwise turning corresponds to a positive θ and vice versa (see Fig. 2). Thus, θ can be deemed as a yaw angle relative to the orbit plane. The aerodynamic acceleration $\boldsymbol{a}_d$ follows the normal vector $\boldsymbol{n}$ of solar panels when ignoring the aerodynamic force experienced by the box component. Therefore

$$a_d = \|\boldsymbol{a}_d\| = \frac{C_d q S_r}{m}, \tag{2}$$

where C_d is the drag coefficient, $q = \rho {v_r}^2/2$ is the dynamic pressure, $\rho = \rho(h)$ is the atmospheric density at a height h (refer to Eq. (1)), S_r is the vehicle reference area, and m is its mass. We use Newton's sine-squared law to derive the drag coefficient [35]

$$C_d = C_{d_0} (\cos\theta)^2, \tag{3}$$

where C_{d_0} is the drag coefficient for $\theta = 0$.

The governing equations of the spacecraft motion in the BME@t_0 frame are

$$\ddot{\boldsymbol{r}} + \frac{Gm_p}{r^3}\boldsymbol{r} + Gm_s\left(\frac{\boldsymbol{r}_s}{r_s^3} + \frac{\boldsymbol{r}-\boldsymbol{r}_s}{\|\boldsymbol{r}-\boldsymbol{r}_s\|^3}\right) = -\mathcal{Q}_{v\to b}(t)\,\mathcal{R}_y(-\theta)\,\frac{C_{d_0} q S_r (\cos\theta)^2}{m}\,\boldsymbol{i}_n, \tag{4}$$

where $\boldsymbol{r}$ and $\boldsymbol{r}_s$ are the position vectors of the spacecraft and the Sun, respectively, whereas r and r_s are their magnitudes; $\mathcal{R}_y$ is the direction cosine matrix about the y_v-axis; $\boldsymbol{i}_n = [1, 0, 0]^\top$. The orbital parameters of the Sun with respect to Mars are read at initial epoch t_0 via the DE430 ephemeris model [36] and kept invariable during the flight, except for the true anomaly, which is calculated by solving Kepler's equation at each time step [22]. Eq. (4) embeds both multi-body gravity (2nd and 3rd terms on the left-hand side) and aerodynamic forces (right-hand side). By swapping the right-hand term on and off one can obtain the equations for the ballistic capture as special case.

3. Methodology

The dynamical model described by Eq. (4) involves both orbital and aerodynamics. In order to construct orbits that exploit both components, an ad hoc method is proposed. Figure 3 outlines the whole insertion process. Firstly, the spacecraft approaches Mars from a far distance with attractions from the Sun and Mars (*pre-capture*, $t < t_0$). At t_0, the spacecraft experiences the first close encounter, where it exerts a small periapsis maneuver Δv_0, which yields a relatively stable orbit. The subsequent phase (*aerobraking phase*, $t > t_0$) is characterized by three-body orbits alternating a series of atmospheric passages at periapsis and trim maneuvers at apoapsis (Δv_j at $t = t_j$). At $t = t_f$, a periapsis raising maneuver (Δv_f) is performed to target the science orbit (*mission phase*, $t > t_f$).

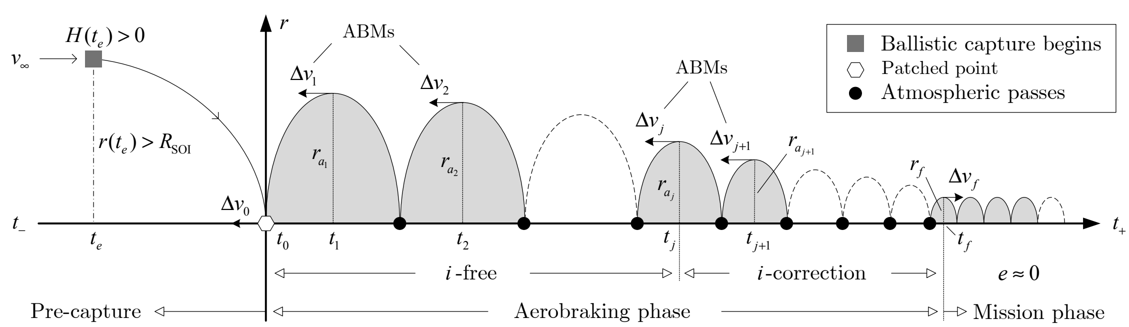

Figure 3: Layout of the whole insertion process (t: time, r: distance to Mars).

3.1. Pre-capture Phase

A method preliminary described in Hyeraci and Topputo [33] and later generalized in Luo et al. [20] is employed to generate ballistic capture orbits. It is briefly outlined as follows.

3.1.1. Initial Conditions and Orbit Classification

Initial conditions (i.c.) at t_0 are defined by specifying initial periapsis radius r_0, eccentricity e_0, inclination i_0, right ascension of the ascending node (RAAN) Ω_0, argument of periapsis ω_0, and true anomaly f_0 in the BME@t_0. Without loss of generality, we assume the spacecraft initially located at the periapsis of an osculating ellipse around Mars, i.e., $f_0 = 0$; the eccentricity of this ellipse is such that $e_0 \in [0.9, 1)$ [33, 37]. Orbital inclination i_0 is chosen arbitrary, and a fixed $\omega_0 \in [0, 2\pi)$ is taken. Thus, two orbital elements, namely the periapsis radius and RAAN, are left free. We discretize them with $r_0 \in [r_{0l}, r_{0h}]$ and $\Omega_0 \in [0, 2\pi)$ into N_{r_0} and N_{Ω_0} points, respectively, where r_{0l} corresponds to an altitude outside of Martian atmosphere and r_{0h} is an upper bound.

Before orbital integrations, we introduce an escape criterion. The spacecraft escapes from Mars at time t_e if the following two conditions are simultaneously satisfied [20],

$$H(t_e) > 0, \qquad r(t_e) > R_{\mathrm{SOI}}, \tag{5}$$

where R_{SOI} is in Table 1 and H is the Kepler energy of the spacecraft with respect to Mars,

$$H(t) = \frac{v^2(t)}{2} - \frac{Gm_p}{r(t)}. \tag{6}$$

The function $H(t)$ is not constant due to the perturbation from the Sun.

The motion of the spacecraft is obtained by forward and backward integration of the i.c. under Eq. (4) (with right-hand side set to zero). According to their orbital behaviors, the i.c. are classified into different sets [20, 22]. The focus is on two of them, i.e.,

1) Weakly Stable Set, $\mathcal{W}_n$ ($n \geq 1$): contains i.c. whose orbits perform n complete revolutions about Mars without impacting with or escaping from it when integrating forward in time;

2) Unstable Set, $\mathcal{X}_{-1}$: contains i.c. whose orbits escape from Mars without completing any revolution around or impacting with it when integrating backward in time.

3.1.2. Construction and Ranking of Ballistic Capture Orbits

The capture set, a set containing i.c. associated to ballistic capture orbits, is derived through

$$\mathcal{C}^n_{-1} = \mathcal{X}_{-1} \cap \mathcal{W}_n. \tag{7}$$

Starting from the i.c. in $\mathcal{C}^n_{-1}$, a spacecraft can: 1) escape Mars in backward time ($\mathcal{X}_{-1}$), or equivalently approach it in forward time, and 2) perform at least n natural revolutions about Mars ($\mathcal{W}_n$); refer to Hyeraci and Topputo [33] and Luo et al. [20] for details.

In general, the capture set $\mathcal{C}_{-1}^{n}$ embodies a number of points. Solutions with regular post-capture behaviors are favorable in applied scenarios as they can offer multiple repetitive insertion conditions (*ideal* orbits). A stability index $\mathcal{S}$ is introduced in Luo et al. [20], that is

$$\mathcal{S} = \frac{t_n - t_0}{n}, \tag{8}$$

where t_n is the time at which the n-th revolution is accomplished. Physically, the value of $\mathcal{S}$ depicts the mean orbital period in n revolutions [20, 22, 38].

3.2. Aerobraking Phase

3.2.1. Periapsis Maneuver and Aerobraking Trim Maneuvers

A small periapsis braking maneuver is employed at the first close encounter, $r_0 = r(t_0)$. This is twofold: a) It shortens the total aerobraking duration; and b) It provides a geometry that favors the convergence of the subsequent aerobraking targeting algorithm. While Eq. (7) yields low-energy Mars-approaching orbits, the n revolutions past t_0 guaranteed by $\mathcal{C}_{-1}^{n}$ are not actually performed, yet kept as backup option in case of a single-point propulsion failure.

Let v_0 be the spacecraft velocity at t_0, and let r_{a_0} be a target apoapsis distance after performing Δv_0. The cost of the periapsis tangential maneuver is then

$$\Delta v_0 = \left| \sqrt{2Gm_p \left(\frac{1}{r_0} - \frac{1}{r_0 + r_{a_0}} \right)} - v_0 \right|, \tag{9}$$

which is found with a standard two-body dynamics.

Aerobraking trim maneuvers (ABMs) at apoapses, if necessary, are used to ensure atmospheric pass conditions. The dynamic pressure at periapsis (denoted by q_p) is selected as the targeting parameter of each ABM, as done in the MGS, Magellan, and Venus Express missions [7, 11, 12, 39]. Algorithm 1 presents the procedure to compute the ABMs Δv_j, where r_{p_0} is a given value ($j = 1$) or it is retrieved from previous iteration ($j \geq 2$), $\bar{q}_p$ is the required periapsis dynamic pressure, and $\delta \bar{q}_p$ is its tolerance.

In summary, following the periapsis maneuver Δv_0, a number of atmospheric passages are used to gradually reduce the orbit altitude, with ABMs Δv_j interposed at apoapses, if needed (see Fig. 3). A semi-analytical method is used to estimate the aerobraking duration; see the Appendix.

3.2.2. Orbital Inclination Correction

A yawed attitude during aerobraking is proposed to correct the orbital inclination perturbed by the Sun gravity. It is then natural to question whether the inclination

Algorithm 1 Algorithm to target a required periapsis dynamic pressure

function TargetDeltaV(r_{p_0}, $\bar{q}_p$, $\delta\bar{q}_p$)
    Set $r_p = r_{p_0}$
    for $k = 1 \rightarrow 10$ **do**
        Target r_p by adjusting apoapsis velocity v_{a_j} with Δv_j
        Calculate periapsis dynamic pressure q_p
        if $|q_p - \bar{q}_p| < \delta\bar{q}_p$ **then**
            Break
        else
            $r_p \leftarrow r_p - H \ln(\bar{q}_p / q_p)$
        end if
    end for
    $r_{p_0} \leftarrow r_p$
    return Δv_j and r_{p0}
end function

should be corrected as early as possible, when the orbit is large and elongated. Answering this question drives the following arguments.

A yaw angle θ decomposes the aerodynamic acceleration a_d. The inclination rate of change is derived by using Gauss's equations [1]

$$\frac{\mathrm{d}i}{\mathrm{d}t} = \frac{\sqrt{1-e^2}\cos u}{na(1+e\cos f)} a_n, \tag{10}$$

where $u = \omega + f$ is the argument of latitude, a_n is the normal component of the aerodynamic acceleration; see Eq. (A1) for definitions of remaining parameters. We assume $\theta \neq 0$. From Eqs. (3), (4), and (A2),

$$a_n = a_d\,(\cos\theta)^2 \sin\theta = \frac{cGm_p\rho A(1+2e\cos f+e^2)}{2a(1-e^2)}, \tag{11}$$

where $c = (\cos\theta)^2 \sin\theta$. Following the derivation in the Appendix, the derivative of i with respect to the eccentric anomaly E reads

$$\frac{\mathrm{d}i}{\mathrm{d}E} = \frac{c\rho a A\cos u(1-e^2\cos^2 E)}{2\sqrt{1-e^2}}. \tag{12}$$

Using Eqs. (A4), (A8) and $\cos u = \cos\omega\cos f - \sin\omega\sin f$, Eq. (12) becomes

$$
\begin{aligned}
\frac{\mathrm{d}i}{\mathrm{d}E} =& \frac{c\rho_0 aA\cos\omega(1+e\cos E)(\cos E - e)\exp\left[-\kappa(1-\cos E)\right]}{2\sqrt{1-e^2}} \\
&- \frac{c\rho_0 aA\sin\omega\sin E(1+e\cos E)\exp\left[-\kappa(1-\cos E)\right]}{2},
\end{aligned}
\tag{13}
$$

where ω is the argument of periapsis. Note that the integral over a revolution of the second term in the right-side of Eq. (13) is zero due to the odd function $\sin E$. Referring to Eq. (A10), the inclination change after one revolution is [40]

$$
\begin{aligned}
\Delta i = \int_{-\pi}^{\pi}\frac{\mathrm{d}i}{\mathrm{d}E}\mathrm{d}E \approx c\rho_0 aA\cos\omega\int_{-\pi}^{\pi}\frac{(1+e\cos E)(\cos E - e)}{2\sqrt{1-e^2}}\exp\left(-\kappa\frac{E^2}{2}\right)\mathrm{d}E \\
\approx c\rho_0 aA\cos\omega\sqrt{1-e^2}\int_{-\infty}^{\infty}\exp\left(-\kappa\frac{E^2}{2}\right)\mathrm{d}E = c\rho_0 aA\cos\omega\sqrt{1-e^2}\sqrt{\frac{\pi}{2\kappa}}.
\end{aligned}
\tag{14}
$$

Thus, the average rate of change of inclination over a revolution takes the form

$$
\frac{\overline{\mathrm{d}i}}{\mathrm{d}t} = \frac{\rho_0 C_{d_0} S_r\cos\omega\,(\cos\theta)^2\sin\theta}{ma}\sqrt{\frac{Gm_p H\,(1-e^2)}{\pi e}}. \tag{15}
$$

From Eq. (15), $\overline{\mathrm{d}i}/\mathrm{d}t$ depends on values of ρ_0, ω, e, and a, the latter playing a dominant role. That is, the smaller a, the higher the average rate $\overline{\mathrm{d}i}/\mathrm{d}t$. This indicates that a late inclination correction via yaw maneuver is desirable.

After the aerobraking phase, an apoapsis maneuver Δv_f is employed to raise the periapsis above the atmosphere and thus to deploy the spacecraft into the final operative orbit (see Fig. 3).

3.3. Optimizing the Yaw Angle

Using Eqs. (3), (4) and (A12) yields

$$
\frac{\overline{\mathrm{d}a}}{\mathrm{d}t} = -\frac{\rho_0 C_{d_0} S_r(\cos\theta)^3}{m}\left[\frac{Gm_p H\,(1+e)^3}{2\pi e(1-e)}\right]^{\frac{1}{2}}. \tag{16}
$$

From Eq. (16), it can be inferred that $\overline{\mathrm{d}a}/\mathrm{d}t$ is domniated by θ, and varies continuously with it. Following analogous derivation of Eq. (15), it is possible to obtain

$$
\frac{\overline{\mathrm{d}\Omega}}{\mathrm{d}t} = \frac{\rho_0 C_{d0} S_r\sin\omega\,(\cos\theta)^2\sin\theta}{ma\sin i}\sqrt{\frac{Gm_p H\,(1-e^2)}{\pi e}} \tag{17}
$$

and

$$\overline{\frac{\mathrm{d}\omega}{\mathrm{d}t}} = -\cos i\,\overline{\frac{\mathrm{d}\Omega}{\mathrm{d}t}}. \tag{18}$$

Through Eqs. (17) and (18) it is possible to infer that the condition $\overline{\mathrm{d}\omega}/\mathrm{d}t = 0$ can be achieved either by using polar orbits ($i = \pi/2$) or by choosing $\omega = 0$ or π. In all these cases, ω is preserved, consistently with the subsequent derivation of orbital inclination.

The focus is now on selecting the value of yaw angle θ and semi-major axis a_θ where the i-correction begins. Observing that the in-plane and out-of-plane orbital variations, or equivalently $\overline{\mathrm{d}a}/\mathrm{d}t$ and $\overline{\mathrm{d}i}/\mathrm{d}t$ are both affected by θ (Eqs. (15) and (16)), a natural choice would be to select an initial a_θ that makes it possible to attain both targets simultaneously. Following this approach, dividing Eq. (15) by Eq. (16) produces

$$\overline{\mathrm{d}i} = -\frac{\tan\theta\cos\omega\,(1-e)}{2a(1+e)}\,\overline{\mathrm{d}a}. \tag{19}$$

It is possible to integrate both sides of Eq. (19), i.e.,

$$\int_{i_\theta}^{i_f} \overline{\mathrm{d}i} = -\int_{a_\theta}^{a_f} \frac{\tan\theta\cos\omega\,(1-e)}{2a(1+e)}\overline{\mathrm{d}a}, \tag{20}$$

where i_θ, a_θ are the initial inclination, semi-major axis, while i_f, a_f are their required targets. Then, substituting $r_p = a(1-e)$ in Eq. (20) and considering that the aim is finding a policy involving constant θ, one gets

$$\int_{i_\theta}^{i_f} \overline{\mathrm{d}i} = -\frac{r_p\tan\theta\cos\omega}{2}\int_{a_\theta}^{a_f} \frac{1}{2a^2 - ar_p}\overline{\mathrm{d}a}, \tag{21}$$

where ω is assumed constant by setting $i \approx \pi/2$ and/or $\omega = 0$ or π. Assuming constant r_p allows integrating Eq. (21):

$$i_f - i_\theta = \tan\theta\cos\omega\left[\tanh^{-1}\left(\frac{4a_f}{r_p} - 1\right) - \tanh^{-1}\left(\frac{4a_\theta}{r_p} - 1\right)\right]. \tag{22}$$

In Eq. (22), a_θ is the unknown, which is function of θ, while i_θ, i_f, and a_f are treated as input values, and ω and r_p are known. That is, there are infinite pairs of a_θ and θ that allow reaching a_f and i_f simultaneously.

3.3.1. Minimum yawing duration

The rationale is choosing a yaw angle that involves the minimum yawed duration. This leads to an optimized yaw angle $\bar{\theta}$ and its corresponding semi-major axis $a_{\bar{\theta}}$. To ease the notation, we define

$$\Xi = -\sqrt{\frac{2H}{\pi G m_p}} \frac{\bar{q}_p C_{d0} S_r}{m} \tag{23}$$

and

$$\mathcal{F}(a_\theta) = \tanh^{-1}\left(\frac{4a_f}{r_p} - 1\right) - \tanh^{-1}\left(\frac{4a_\theta}{r_p} - 1\right). \tag{24}$$

From Eqs. (16), (A12) and (A16), it is possible to obtain the estimated yawing duration when $\theta \neq 0$, i.e.,

$$\Delta t_\theta = \frac{\int_{a_\theta}^{a_f} \mathcal{G}(a)\, \overline{\mathrm{d}a}}{\Xi (\cos\theta)^3}. \tag{25}$$

Using Eq. (25) and the chain rule, we calculate

$$\frac{\mathrm{d}\Delta t_\theta}{\mathrm{d}a_\theta} = \frac{3\sin\theta \int_{a_\theta}^{a_f} \mathcal{G}(a)\overline{\mathrm{d}a}}{\Xi(\cos\theta)^4}\frac{\mathrm{d}\theta}{\mathrm{d}a_\theta} - \frac{\mathcal{G}(a_\theta)}{\Xi(\cos\theta)^3} = \frac{1}{\Xi(\cos\theta)^3} \underbrace{\left[3\tan\theta \int_{a_\theta}^{a_f} \mathcal{G}(a)\overline{\mathrm{d}a}\frac{\mathrm{d}\theta}{\mathrm{d}a_\theta} - \mathcal{G}(a_\theta)\right]}_{\mathcal{L}(a_\theta)}, \tag{26}$$

where $\mathrm{d}\theta/\mathrm{d}a_\theta$ can be derived from Eq. (22),

$$\frac{\mathrm{d}\theta}{\mathrm{d}a_\theta} = -\frac{4\Delta i \cos\omega}{r_p \left\{\Delta i^2 + \left[\mathcal{F}(a_\theta)\right]^2 (\cos\omega)^2\right\} \left[\left(\frac{4a_\theta}{r_p} - 1\right)^2 - 1\right]} \tag{27}$$

and $\Delta i = i_f - i_\theta$.

Considering that $|\theta| < \pi/2$ and $\Xi \neq 0$, the yawed duration Δt_θ arrives an extremum when $\mathrm{d}\Delta t_\theta/\mathrm{d}a_\theta = 0$, or equivalently, when $\mathcal{L}(a_{\bar{\theta}})$ in Eq. (26) is zero. Enforcing $\mathcal{L}(a_{\bar{\theta}}) = 0$ and using Eq. (27) yields

$$-\frac{12\Delta i^2 \int_{a_{\bar{\theta}}}^{a_f} \mathcal{G}(a)\, \overline{\mathrm{d}a}}{r_p \mathcal{F}(a_{\bar{\theta}}) \left\{\Delta i^2 + \left[\mathcal{F}(a_{\bar{\theta}})\right]^2 (\cos\omega)^2\right\} \left[\left(\frac{4a_{\bar{\theta}}}{r_p} - 1\right)^2 - 1\right]} - \mathcal{G}(a_{\bar{\theta}}) = 0. \tag{28}$$

Newton's method is introduced to solve Eq. (28), while the current apoapsis distance is used as an initial guess of a_θ in Eq. (24). An optimal $a_{\bar{\theta}}$ with respect to minimum yawing duration is obtained by verifying an additional condition: the second-order derivative $\mathrm{d}^2\Delta t_\theta/\mathrm{d}a_\theta^2 > 0$. The corresponding yaw angle $\bar{\theta}$ is then computed by Eq. (22).

3.3.2. Minimum aerobraking duration

While $\bar{\theta}$ ensures the shortest yawing phase duration, it would be also desirable to find another yaw angle $\hat{\theta}$ that guarantees an overall minimum aerobraking duration. By using Eqs. (A16) and (25), the aerobraking duration can be written as

$$\Delta t = \underbrace{\frac{\int_{a_0}^{a_\theta} \mathcal{G}(a)\,\overline{\mathrm{d}a}}{\Xi}}_{\theta=0} + \underbrace{\frac{\int_{a_\theta}^{a_f} \mathcal{G}(a)\,\overline{\mathrm{d}a}}{\Xi\,(\cos\theta)^3}}_{\theta\neq 0}, \tag{29}$$

where a_0 is the semi-major axis after Δv_0. Similarly to Eq. (26), we compute the derivative of Δt with respect to a_θ

$$\begin{aligned}\frac{\mathrm{d}\Delta t}{\mathrm{d}a_\theta} =& \frac{\mathcal{G}(a_\theta)}{\Xi} + \frac{3\sin\theta\int_{a_\theta}^{a_f}\mathcal{G}(a)\overline{\mathrm{d}a}}{\Xi(\cos\theta)^4}\frac{\mathrm{d}\theta}{\mathrm{d}a_\theta} - \frac{\mathcal{G}(a_\theta)}{\Xi(\cos\theta)^3} \\ =& \frac{1}{\Xi(\cos\theta})^3 \underbrace{\left\{3\tan\theta\int_{a_\theta}^{a_f}\mathcal{G}(a)\overline{\mathrm{d}a}\,\frac{\mathrm{d}\theta}{\mathrm{d}a_\theta} - \mathcal{G}(a_\theta)\left[1-(\cos\theta)^3\right]\right\}}_{\mathcal{M}(a_\theta)}.\end{aligned} \tag{30}$$

Using Eq. (27) and imposing $\mathcal{M}(a_\theta) = 0$, the following is obtained

$$-\frac{12\Delta i^2\int_{a_{\hat{\theta}}}^{a_f}\mathcal{G}(a)\overline{\mathrm{d}a}}{r_p\mathcal{F}\left(a_{\hat{\theta}}\right)\left\{\Delta i^2 + \left[\mathcal{F}\left(a_{\hat{\theta}}\right)\right]^2(\cos\omega)^2\right\}\left[\left(\frac{4a_{\hat{\theta}}}{r_p}-1\right)^2-1\right]} - \left[1-(\cos\hat{\theta})^3\right]\mathcal{G}(a_{\hat{\theta}}) = 0 \tag{31}$$

and

$$\hat{\theta} = \tan^{-1}\frac{\Delta i}{\mathcal{F}(a_{\hat{\theta}})\cos\omega}. \tag{32}$$

By solving Eqs. (31), (32) and $\mathrm{d}^2\Delta t_\theta/\mathrm{d}a_\theta^2$ numerically it is possible to obtain the critical semi-major axis $a_{\hat{\theta}}$ that corresponds to a minimum aerobraking duration, and hence an optimal yaw angle $\hat{\theta}$.

3.3.3. Summary of the approach

The full procedure developed to constructing ballistically captured and atmospheric braked Mars orbits is summarized in Algorithm 2. The computation of a_θ is only activated when $r_{a_j} < 5R$ and $a_j \geq a_{\bar{\theta}}$ (or $a_{\hat{\theta}}$); that is to say, θ is updated by $\bar{\theta}$ (or $\hat{\theta}$) and fixed once $a_j < a_{\bar{\theta}}$ (or $a_{\hat{\theta}}$). This strategy speeds up the numerical simulations. The $5R$ criterion has been chosen through numerical experiments.

Algorithm 2 Outline of Mars orbit insertion via ballistic capture and aerobraking

Initialize spacecraft's parameters m_0, C_{d_0}, S_r, and specific impulse I_{sp}
Initialize Martian density model with ρ_0, h_0, and H
Set aerobraking targeting variables r_{p_0}, $\bar{q}_p$, and $\delta\bar{q}_p$
Set a zero-yawed attitude with $\theta = 0$ and an inclination mode with $i_{\text{flag}} = 1$
Choose periapsis epoch t_0, r_f and i_f according to mission requirements
Give e_0 and ω_0; set $i_0 = i_f$, $f_0 = 0$; discretize r_0 and Ω_0 into N_{r_0} and N_{Ω_0} points
Integrate (4) forward and backward with a zero right-hand side
Obtain sets $\mathcal{X}_{-1}$ and $\mathcal{W}_n$; generate capture set $\mathcal{C}_{-1}^n = \mathcal{X}_{-1} \cap \mathcal{W}_n$
Extract candidates from $\mathcal{C}_{-1}^n$ having low values of stability index $\mathcal{S}$
Calculate Δv_0 with (9) and a predefined r_{a_0}; update m with rocket equation
Integrate (4) until next apoapsis with a distance r_{a_1} (see Fig. 3)
$j = 1$
while $r_{a_j} > r_f$ **do**
    if $i_{\text{flag}} = 1$ **and** $r_{a_j} < 5R$ **then**
        Compute $a_{\bar{\theta}}$ (or $a_{\hat{\theta}}$) and $\bar{\theta}$ (or $\hat{\theta}$) by solving (28) (or (31)) and (22)
        $a_j = 0.5(r_{p0} + r_{a_j})$
        if $a_{a_j} < a_{\bar{\theta}}$ (or $a_{\hat{\theta}}$) **then**
            $\theta \leftarrow \bar{\theta}$ (or $\hat{\theta}$)
            Set $i_{\text{flag}} = 0$
        end if
    end if
    $[\Delta v_j, r_{p0}] = \textsc{TargetDeltaV}(r_{p0}, \bar{q}_p, \delta\bar{q}_p)$ (see Algorithm 1)
    Update m with the rocket equation
    $j = j + 1$
    Integrate (4) until next apoapsis with r_{a_j} and v_{a_j}
end while
Compute Δv_f with r_{a_j}, v_{a_j} and $e_f = 0$
Compute $\Delta v = \Delta v_0 + \sum \Delta v_j + \Delta v_f$
Compare obtained r_f and i_f with required values

4. Simulations

4.1. Mars ballistic capture approach

A MGS-like vehicle with $m_0 = 760$ kg, $S_r = 17.04$ m^2, $C_{d0} = 1.95$, and $I_{sp} = 300$ s, is considered [2, 7]. The periapsis dynamic pressure $\bar{q}_p$ is 0.6 N/m^2, following the original plan of the MGS mission [2, 7]. The tolerance $\delta\bar{q}_p$ is 0.02 N/m^2 and can be reached in few iterations. An initial reference periapsis distance is $r_{p0} = R + 100$ km. The final operative orbit is a circular orbit with an altitude of 300 km ($r_f = R + 300$ km) and an inclination of 90 degree (i_f). A polar orbit is chosen to support the hypothesis of constant ω (see Sec. 3.3).

The initial condition is: 1) $t_0 = 2459137$ JD (or 14 Oct 2020), when Mars has a true anomaly of $\pi/4$ about the Sun; this favours the chances of gravitational capture [22, 37, 41]; 2) $e_0 = 0.99$; this is larger than 0.95 used in Hyeraci and Topputo [41] and Luo et al. [20] because it lowers r_0 in the capture set $\mathcal{C}^n_{-1}$ and thus reduces the apoapsis trim maneuver Δv_1 (see Fig. 3); 3) $i_0 = i_f = 90$ deg; 4) $\omega_0 = 330$ deg; 5) $r_0 \in [130 \text{ km} + R,\ 2R]$ (a minimum altitude of 130 km guarantees that the periapsis maneuver Δv_0 occurs outside of the Martian atmosphere) and $\Omega_0 \in [0,\ 2\pi)$ are uniformly discretized into $N_{r_0} = 653$ and $N_{\Omega_0} = 720$ points, respectively. This is different from fixing Ω_0 in Luo et al. [20] and Luo and Topputo [38], because a large $\cos\omega_0$ is beneficial to inclination corrections (see Eqs. (15) and (22)). A value of $n = 6$ is taken; that is, backup ballistic capture orbits in $\mathcal{C}^6_{-1}$ will perform at least 6 free revolutions about Mars (after t_0).

The computation of the capture set takes 1.8 hours with 6-core Intel i7 CPU (2.60 GHz) architecture and Matlab environment. Figure 4(a) shows solutions belonging to $\mathcal{C}^6_{-1}$ projected onto the plane of the pre-capture duration ($t_0 - t_e \leq 350$ days) and the post-capture stability index ($\mathcal{S} \leq 160$ days). As for $t_0 - t_e$, the shorter, the better. Low values of $\mathcal{S}$ are associated to regular post-capture orbits [20, 22, 38]. Desirable solutions are thus orbits in $\mathcal{C}^6_{-1}$ having short $t_0 - t_e$ and low $\mathcal{S}$; however, these two conditions are clearly in antithesis. Looking closely at Fig. 4(a), a sample (indicated by the arrow) is taken from the island at $t_0 - t_e \in [200,\ 250]$ day and $\mathcal{S} \leq 120$ day, although we have found that the subsequent aerobraking is not sensitive to which sample we choose. In practice, orbits of interest can be extracted from $\mathcal{C}^6_{-1}$ by following multiple criteria depending on mission requirements. Figure 4(b) presents the sample ballistic capture orbit in the BME@t_0 frame. The distance and inclination profiles are illustrated in Fig. 5. It can be seen that the post-capture altitude is regular and repetitive (Fig. 5(a)). The inclination has instead large variations owing to out-of-plane perturbations from the Sun (Fig. 5(b)). This involves inclination corrections described in Section 3.2.2.

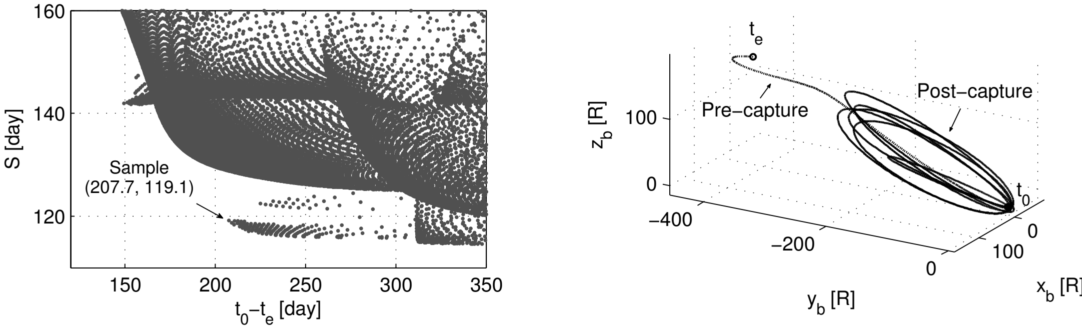

(a) $t_0 - t_e$ vs $\mathcal{S}$ (b) Sample ballistic capture orbit

Figure 4: Pre-capture duration vs stability index for solutions in $\mathcal{C}_{-1}^{6}$ and sample orbit.

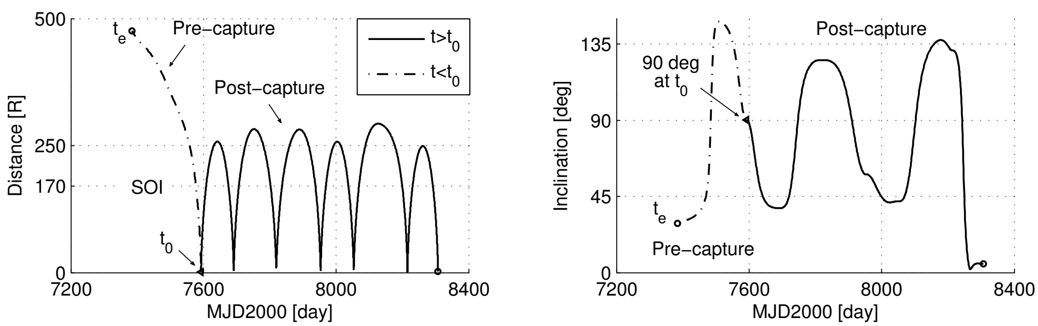

(a) Distance to Mars (b) Inclination to Martian equator

Figure 5: Distance and inclination profiles of the sample solution in Fig. 4.

4.2. Post-capture trim maneuvers and aerobraking

Let us focus on the periapsis maneuver at t_0. To allow independent reproduction of the results, the state at t_0 (and at other four subsequent epochs) is reported in Table 2. A moderate r_{a_0} balancing perturbation effects and fuel consumption is adopted: $r_{a_0} = 160R$, slightly less than the SOI of 170 radii (see Table 1). Therefore $\Delta v_0 = 7.2$ m/s by Eq. (9); see Fig. 6(a). The apoapsis distance at t_1 (the first apoapsis of the aerobraking phase; see Fig. 3) is $r_{a_1} = 159.5R$ (see Fig. 6(b)), quite close to the desired value of r_{a_0}. After Δv_0, the ABMs Δv_j ($j = 1, 2, ...$) are calculated by Algorithm 1, as noted in Fig. 6(a). The largest impulse is $\Delta v_1 = 7.8$ m/s; from then on, the ABMs are less than 2 m/s. Figure 6(c) shows the inclination variations. It can be seen that the inclination becomes stable when Mars plays a major role on the orbit.

Table 2: State parameters at t_0, t_j and t_f (before performing maneuvers); $\bar{\theta}$: minimum yawing duration; $\hat{\theta}$: minimum aerobraking duration.

Epoch (JD)	Position (km)			Velocity (km/s)			Loop	h	i
	x_b	y_b	z_b	v_{xb}	v_{yb}	v_{zb}	No. (j)	km	degree
2459137.000, t_0	-886.2	3838.7	-2274.6	-0.487	2.109	3.748	0	1155.0	90.00
2459548.181, $t_j(\bar{\theta})$	1498.6	-6190.3	3628.5	0.591	-0.827	-1.654	204	3936.0	80.22
2459589.250, $t_f(\bar{\theta})$	756.0	-3124.1	1817.7	0.393	-1.605	-2.922	589	**298.5**	**89.93**
2459543.342, $t_j(\hat{\theta})$	1957.5	-8084.7	4737.6	0.470	-0.658	-1.318	174	6178.6	80.22
2459586.766, $t_f(\hat{\theta})$	750.9	-3100.9	1830.8	0.392	-1.629	-2.920	523	**284.3**	**90.02**

When the condition $r_{a_j} < 5R$ is achieved, the optimized $a_{\bar{\theta}}$ and corresponding $\bar{\theta}$ (or $a_{\hat{\theta}}$ and corresponding $\hat{\theta}$) is solved and updated at each apoapsis (see Algorithm 2). The spacecraft holds a zero-yawed angle until $a_{aj} < a_{\bar{\theta}}$ (or $a_{aj} < a_{\hat{\theta}}$); subsequently, a yawed attitude with $\bar{\theta}$ (or $\hat{\theta}$) is maintained during atmospheric passages. For convenience the apoapsis epoch activating a yawed attitude is denoted by $t_j(\bar{\theta})$ (or $t_j(\hat{\theta})$). The states at t_j, as well as the altitude and inclination, are given in Table 2. In this simulation, $\bar{\theta} = 55.0$ degree and $\hat{\theta} = 48.1$ degree; see Fig. 6(d). The inclination after t_j is gradually adjusted from 80.22 degree to the target i_f for both optimization options (see Table 2 and Fig. 6(c)). The zoomed-up view in Fig. 6(b) clearly shows the reduction of $\mathrm{d}a/\mathrm{d}t$ when $\theta \neq 0$.

The aerobraking ends when $r_{a_j} < r_f$; the corresponding state is also given in Table 2. The results show that: 1) both in-plane (altitude) and out-of-plane (inclination) dynamics can simultaneously attain their targets within an acceptable

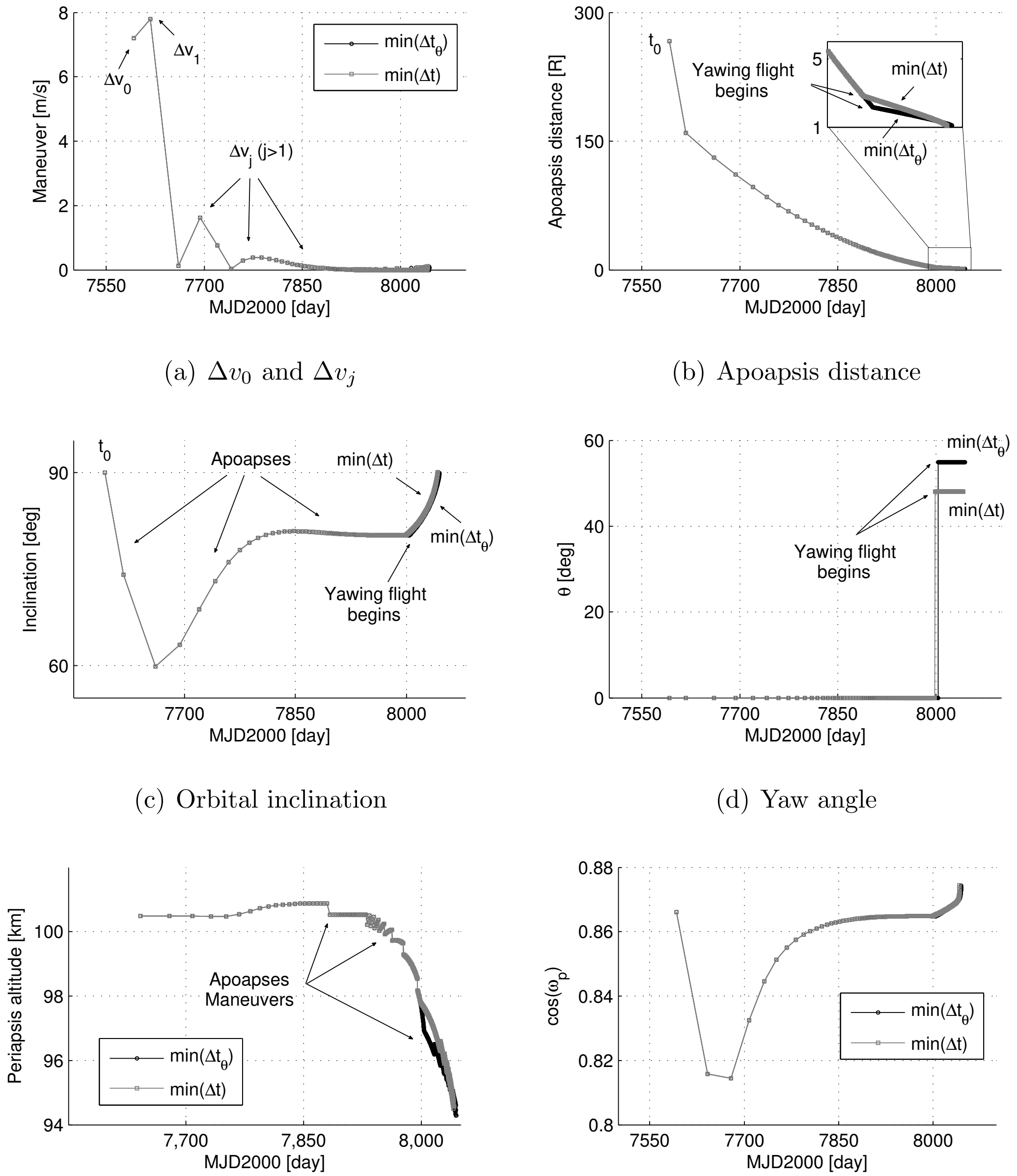

(a) Δv_0 and Δv_j

(b) Apoapsis distance

(c) Orbital inclination

(d) Yaw angle

(e) Periapsis altitude

(f) $\cos \omega_p$

Figure 6: Parameter histories of the insertion orbit.

tolerance; 2) the two optimization approaches are verified, i.e., $t_f(\bar{\theta}) - t_j(\bar{\theta}) = 41.1$ day and $t_f(\hat{\theta}) - t_j(\hat{\theta}) = 43.4$ day; $t_f(\bar{\theta}) - t_0 = 452.3$ day and $t_f(\hat{\theta}) - t_0 = 449.8$ day. Figure 6(e) shows the pericenter height during the aerobraking phase. The variation is so negligible that r_p can be treated as constant, as already done in Eq. (A13). In practice, an altitude less than 100 km may be dangerous. This risk can be avoided or reduced by: 1) lowering the targeting $\bar{q}_p$; 2) increasing the reference area S_r; or 3) estimating and updating atmospheric and spacecraft parameters during previous aerobraking phase. Figure 6(f) shows the cosine value of argument of periapsis. The assumption of a constant ω is verified. Figure 7 plots the capture orbit with the optimization condition of $\min(\Delta t_\theta)$ together with the ballistic capture orbit. The close-up view in Fig. 7(b) shows the transition from $\theta = 0$ to $\bar{\theta}$.

4.3. Comparison with other injection options

Table 3 reports the comparisons of multiple MOI methods. The full impulsive option results are taken from the MGS mission [2, 7], where $\Delta v_0 = 973$ m/s deploys the spacecraft into a highly elliptical orbit around Mars and $\Delta v_f = 1270$ m/s is the circularization cost at periapsis. The duration $t_f - t_0$ is the period of the elliptical orbit. Using ballistic capture and chemical propulsion (B.C.+Chem.) is another option. For convenience, the ballistic capture orbit resulting from the sample in Fig. 4 is used. A periapsis maneuver $\Delta v_0 = 1423$ m/s at t_0 is used to inject into an orbit with apoapsis and periapsis altitudes of 1155 and 300 km, respectively, where 1155 km is the altitude at t_0 (see Table 2). Similar to the fully impulsive case, $\Delta v_f = 172$ m/s is applied to circularize the orbit. The data for the conventional aerobraking method (Chem.+Aero.) in Table 3 are taken form MGS mission. The maneuvers $\sum \Delta v_j$ and Δv_f are not listed because the mission was redesigned due to solar panel issues [2, 7]. The planned aerobraking duration is 140 day. Eventually, Table 3 reports the results of this work for both optimization options. The discrepancy of Δv_f derives from their different altitudes at t_f. Comparison among different MOI options indicates that the one based on combination of ballistic capture and aerobraking proposed in this paper offers a good fuel consumption, at the expense of a much longer flight time. Moreover, the reduction of hyperbolic excess velocity upon Mars approach is achieved at the cost of targeting a point in the deep space (e.g., the point at t_e in Fig. 4(b)). This comes at a cost [3], and needs to be considered in the overall mission assessment, yet is out of the scopes of the present work.

5. Conclusions

A novel Mars orbit insertion strategy that combines ballistic capture and aerobraking is presented in this work. Mars approaching orbits that support ballistic

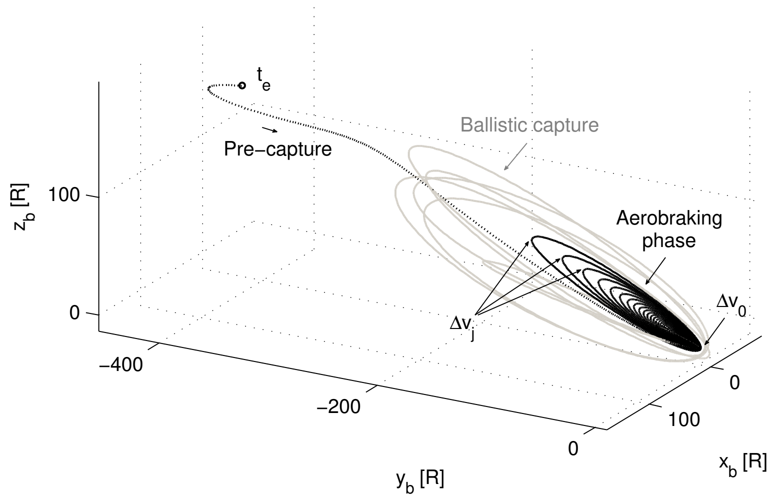

(a) orbit in the BME@t_0 frame (original ballistic capture orbit is superimposed for comparison)

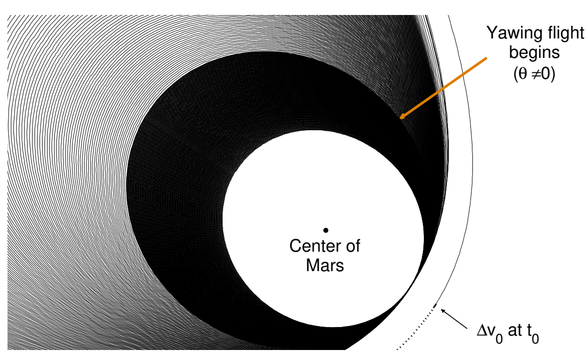

(b) Close-up view

Figure 7: Overall Mars insertion orbit with minimum yawing flight time.

Table 3: Comparison with other MOI types ($\bar{\theta}$: minimum yawing duration; $\hat{\theta}$: minimum aerobraking duration).

MOI type	Total Δv (m/s)	Δv_0 (m/s)	$\sum \Delta v_j$ (m/s)	Δv_f (m/s)	$t_f - t_0$ (day)	$\frac{m_f}{m_0}$
Chemical	2173	973	–	1270	1.9	0.467
B.C.+Chem.	1595	1423	–	172	< 1	0.581
Chem.+Aero.	∼973	973			140	∼0.718
This work ($\bar{\theta}$)	72.2†	7.2	16.2	48.8	452.3	0.976
This work ($\hat{\theta}$)	69.0†	7.2	16.2	45.6	449.8	0.977

† Total Δv of this work excludes the maneuver to enter the pre-capture trajectory and potential expense of station keeping, momentum dumping or other required maneuvers during the aerobraking phase.

capture are first generated using a construction method developed in previous works. A small periapsis maneuver is implemented at the first close passage. A patching point is used to switch to aerobraking. The atmospheric phase features periapsis trim maneuvers and yaw angle tuning to target a prescribed dynamics pressure and inclination, respectively. Comparison with other injection alternatives yields a good compromise of desirable features, i.e., lower insertion fuel consumption, lower failure risks and more flexible launch windows, albeit involving a longer flight time (Mars gravity and atmosphere measurements can be scheduled as by-product of long-time insertion) and more aerobraking trim maneuvers.

Although numerical simulations are carried out in a low-fidelity model, e.g., a point mass assumption for Martian gravity, an exponential model for Martian atmosphere and a simplified "box-wing" configuration for the spacecraft, the developed insertion strategy can be extended to simulating environments modeled with high levels of fidelity and provide an alternative for missions to Mars or other planets/satellites with atmosphere.

Appendix: Aerobraking Duration Prediction

Three assumptions are made: 1) a two-body dynamics is considered; 2) $\theta = 0$; 3) $\bar{q}_p$ is a constant. According to Gauss's equations [1], we obtain

$$\frac{\mathrm{d}a}{\mathrm{d}t} = -\frac{2\sqrt{1 + 2e\cos f + e^2}}{n\sqrt{1 - e^2}} a_d, \tag{A1}$$

where a, e, f, n are the semi-major axis, the eccentricity, the true anomaly, and the mean motion, respectively. The term a_d is the tangential acceleration here; see Eq. (2). Substituting the vis viva equation and $r = \frac{a(1-e^2)}{1+e\cos f}$ into Eq. (2), we have

$$a_d = \frac{Gm_p \rho A(1 + 2e\cos f + e^2)}{2a(1-e^2)}, \tag{A2}$$

where $A = C_{d0}S_r/m$. Using $Gm_p = n^2a^3$, we find that

$$\frac{\mathrm{d}a}{\mathrm{d}t} = -\rho A n a^2 \left[\frac{1 + 2e\cos f + e^2}{1-e^2}\right]^{\frac{3}{2}}. \tag{A3}$$

To calculate the derivatives of a with respect to the eccentric anomaly E, note that

$$\begin{cases} r = a(1 - e\cos E) \\ r\sin f = a\sqrt{1-e^2}\sin E \\ r\cos f = a(\cos E - e) \end{cases}. \tag{A4}$$

Hence, we have

$$\frac{\mathrm{d}E}{\mathrm{d}t} = \frac{n}{1 - e\cos E} \tag{A5}$$

and

$$1 + 2e\cos f + e^2 = \frac{(1-e^2)(1+e\cos E)}{1 - e\cos E}. \tag{A6}$$

There obtains

$$\frac{\mathrm{d}a}{\mathrm{d}E} = -\rho A a^2 \left[\frac{(1+e\cos E)^3}{1 - e\cos E}\right]^{\frac{1}{2}}. \tag{A7}$$

Now assume ρ_0 in Eq. (1) is exactly the density at the pericenter and h_0 is the pericenter altitude. Substituting $r = a(1 - e\cos E)$ into Eq. (1), we can obtain

$$\rho = \rho_0 \exp\left[-\kappa(1 - \cos E)\right] \tag{A8}$$

with $\kappa = \frac{ae}{H}$. Thus,

$$\frac{\mathrm{d}a}{\mathrm{d}E} = -\rho_0 A a^2 \exp\left[-\kappa(1-\cos E)\right] \left[\frac{(1+e\cos E)^3}{1 - e\cos E}\right]^{\frac{1}{2}}. \tag{A9}$$

Since aerobraking occurs in close proximity to the pericenter, we have $1 - \cos E = 2\left(\sin \frac{E}{2}\right)^2 \approx \frac{E^2}{2}$. Then, we evaluate decremental semi-major axis from one apoapsis to next one

$$\begin{aligned}\Delta a = \int_{-\pi}^{\pi} \frac{\mathrm{d}a}{\mathrm{d}E}\mathrm{d}E \approx &- \rho_0 A a^2 \int_{-\pi}^{\pi} \exp\left(-\kappa \frac{E^2}{2}\right) \left[\frac{(1+e\cos E)^3}{1-e\cos E}\right]^{\frac{1}{2}} \mathrm{d}E \\ \approx &- \rho_0 A a^2 \left[\frac{(1+e)^3}{1-e}\right]^{\frac{1}{2}} \int_{-\infty}^{\infty} \exp\left(-\kappa \frac{E^2}{2}\right) \mathrm{d}E.\end{aligned} \tag{A10}$$

Using the Gaussian integral $\int_{-\infty}^{\infty} \exp(-x^2)\mathrm{d}x = \sqrt{\pi}$, Eq. (A10) becomes

$$\Delta a \approx -\rho_0 A a^2 \left[\frac{(1+e)^3}{1-e}\right]^{\frac{1}{2}} \sqrt{\frac{2\pi}{\kappa}}. \tag{A11}$$

Similar conclusions can also be found in Esposito et al. [2], Roy [40] and Zhou and Liu [42]. Dividing Eq. (A11) with $T = 2\pi\sqrt{a^3/Gm_p}$, we obtain the average rate

$$\overline{\frac{\mathrm{d}a}{\mathrm{d}t}} = \frac{\Delta a}{2\pi\sqrt{a^3/Gm_p}} = -\frac{\rho_0 C_{d0} S_r}{m} \left[\frac{Gm_p H (1+e)^3}{2\pi e(1-e)}\right]^{\frac{1}{2}} \tag{A12}$$

and the density at pericenter

$$\rho_0 = \frac{2\bar{q}_p}{v_p^2} = \frac{2\bar{q}_p}{Gm_p(\frac{2}{r_p} - \frac{1}{a})}, \tag{A13}$$

where r_p and v_p are the distance and velocity at pericenter, respectively. The variable r_p is supposed to be constant. Using $r_p = a(1-e)$, we find that e is a single variable function of a. Substituting Eq. (A13) into Eq. (A12) and removing the variable e, we have

$$\overline{\frac{\mathrm{d}a}{\mathrm{d}t}} = -\sqrt{\frac{2H}{\pi G m_p}} \frac{C_{d0} S_r \bar{q}_p}{m} \left[\mathcal{G}(a)\right]^{-1} \tag{A14}$$

and $\mathcal{G}(a)$ is a function of a in the form

$$\mathcal{G}(a) = \sqrt{\frac{a - r_p}{a r_p (2a - r_p)}}. \tag{A15}$$

Now integrating Eq. (A14) from a_j to a_{j+1}, we find that

$$\Delta t = -\frac{m}{C_{d0} S_r \bar{q}_p} \sqrt{\frac{\pi G m_p}{2H}} \int_{a_j}^{a_{j+1}} \mathcal{G}(a) \overline{\mathrm{d}a}. \tag{A16}$$

Numerical integrators are used to solve Eq. (A16) for the aerobraking duration Δt as no explicit integral for $\mathcal{G}(a)$ is found.

Acknowledgements

This work has been supported by the National Natural Science Foundation of China (No. 11602301), the Science and Technology Laboratory on Space Intelligent Control for National Defense (No. KGJZDSYS-2018-12) and the National Key R&D Program of China (No. 2019YFA0706601). We are grateful to Dr. Chen Zhang for supporting the numerical simulations and to Dr. Hanlun Lei for providing helpful opinions.

References

[1] R. H. Battin, An Introduction to the Mathematics and Methods of Astrodynamics, AIAA, New York, 1987.

[2] P. Esposito, V. Alwar, S. Demcak, E. Graat, M. Johnston, R. Mase, Mars Global Surveyor Navigation and Aerobraking at Mars, in: 13th International Conference on Space Flight Dynamics, American Astronautical Society, Greenbelt, MD, 1998, pp. 1–13.

[3] F. Topputo, E. Belbruno, Earth–Mars Transfers with Ballistic Capture, Celestial Mechanics and Dynamical Astronomy 121 (2015) 329–346. doi:10.1007/s10569-015-9605-8.

[4] D. Carrelli, D. O'Shaughnessy, T. Strikwerda, J. Kaidy, J. Prince, R. Powell, Autonomous Aerobraking for Low-cost Interplanetary Missions, Acta Astronautica 93 (2014) 467–474. doi:10.1016/j.actaastro.2012.10.041.

[5] A. Genova, ORACLE: A Mission Concept to Study Mars' Climate, Surface and Interior, Acta Astronautica 166 (2020) 317–329. doi:10.1016/j.actaastro.2019.10.006.

[6] D. A. Spencer, R. Tolson, Aerobraking Cost and Risk Decisions, Journal of Spacecraft and Rockets 44 (2007) 1285–1293. doi:10.2514/1.24303.

[7] D. T. Lyons, J. G. Beerer, P. Esposito, M. D. Johnston, Mars Global Surveyor: Aerobraking Mission Overview, Journal of Spacecraft and Rockets 36 (1999) 307–313.

[8] R. H. Tolson, A. M. Dwyer, J. L. Hanna, G. M. Keating, B. E. George, P. E. Escalera, M. R. Werner, Application of Accelerometer Data to Mars Odyssey Aerobraking and Atmospheric Modeling, Journal of Spacecraft and Rockets 42 (2005) 435–443.

[9] E. Mazarico, M. T. Zube, F. G. Lemoine, D. E. Smith, Atmospheric Density During the Aerobraking of Mars Odyssey from Radio Tracking Data, Journal of Spacecraft and Rockets 44 (2007) 1165–1171. doi:10.2514/1.28448.

[10] K. Uesugi, Results of the MUSES-A "Hiten" Mission, Advances in Space Research 18 (1996) 69–72.

[11] D. T. Lyons, R. Saunders, D. G. Griffith, The Magellan Venus Mapping Mission: Aerobraking Operations, Acta Astronautica 35 (1995) 669–676.

[12] S. Val Serra, O. Bonnamy, O. Witasse, C. Camino, Venus express aerobraking, 18th IFAC World Congress Proceedings 44 (2011) 715–720.

[13] J. C. Smith, J. L. Bell, 2001 Mars Odyssey Aerobraking, Journal of Spacecraft and Rockets 42 (2005) 406–415.

[14] J. E. Graf, R. W. Zurek, J. K. Erickson, B. Jai, M. D. Johnston, R. de Paula, Status of Mars Reconnaissance Orbiter Mission, Acta Astronautica 61 (2007) 44–51. doi:10.1016/j.actaastro.2007.01.032.

[15] H. Renault, N. Sergent, M. Chevallier, N. Kutrowski, A. Bacchetta, D. Temperanza, ExoMars 2016, Orbiter Module Bus a GNC Development Update, CEAS Space Journal 7 (2015) 105–118. doi:10.1007/s12567-014-0070-0.

[16] C. Circi, P. Teofilatto, On the Dynamics of Weak Stability Boundary Lunar Transfers, Celestial Mechanics and Dynamical Astronomy 79 (2001) 41–72. doi:10.1023/A:1011153610564.

[17] C. Circi, Properties of Transit Trajectory in the Restricted Three and Four-Body Problem, Advances in Space Research 49 (2012) 1506–1519. doi:10.1016/j.asr.2012.02.034.

[18] R. Jehn, S. Campagnola, D. García, S. Kemble, Low-Thrust Approach and Gravitational Capture at Mercury, in: Proceedings of the 18th International Symposium on Space Flights Dynamics, volume 584, Munich, Germany, 2004, p. 487.

[19] G. Mingotti, F. Topputo, F. Bernelli-Zazzera, Earth-Mars Transfers with Ballistic Escape and Low-Thrust Capture, Celestial Mechanics and Dynamical Astronomy 110 (2011) 169–188. doi:10.1007/s10569-011-9343-5.

[20] Z.-F. Luo, F. Topputo, F. Bernelli-Zazzera, G.-J. Tang, Constructing Ballistic Capture Orbits in the Real Solar System Model, Celestial Mechanics and Dynamical Astronomy 120 (2014) 433–450. doi:10.1007/s10569-014-9580-5.

[21] E. Fantino, G. Gómez, J. J. Masdemont, Y. Ren, A Note on Libration Point Orbits, Temporary Capture and Low-energy Transfers, Acta Astronautica 67 (2010) 1038–1052. doi:10.1016/j.actaastro.2010.06.037.

[22] Z.-F. Luo, F. Topputo, Analysis of Ballistic Capture in Sun-Planet Models, Advances in Space Research 56 (2015) 1030–1041. doi:10.1016/j.asr.2015.05.042.

[23] K. A. Bokelmann, R. P. Russell, Halo Orbit to Science Orbit Captures at Planetary Moons, Acta Astronautica 134 (2017) 141–151. doi:10.1016/j.actaastro.2017.01.035.

[24] Y. Qi, A. de Ruiter, Low-energy Transfers to Long-term Capture in the Earth-Moon System, Acta Astronautica 152 (2018) 836–849. doi:10.1016/j.actaastro.2018.09.019.

[25] Z.-F. Luo, The Role of the Mass Ratio in Ballistic Capture, Monthly Notices of the Royal Astronomical Society, Accepted (2020). doi:10.1093/mnras/staa2366.

[26] S. Carletta, M. Pontani, P. Teofilatto, Dynamics of Three-dimensional Capture Orbits from Libration Region Analysis, Acta Astronautica 165 (2019) 331–343. doi:10.1016/j.actaastro.2019.09.019.

[27] E. Belbruno, J. Miller, Sun-Perturbed Earth-to-Moon Transfers with Ballistic Capture, Journal of Guidance, Control, and Dynamics 16 (1993) 770–775. doi:10.2514/3.21079.

[28] O. Camino, O. Alonso, D. Gestal, J. de Bruin, P. Rathsman, J. Kugelberg, P. Bodin, S. Ricken, R. Blake, P. Voss, L. Stagnaro, SMART-1 Operations Experience and Lessons Learnt, Acta Astronautica 61 (2007) 203–222. doi:10.1016/j.actaastro.2007.01.042.

[29] M. J. Chung, S. J. Hatch, J. A. Kangas, S. M. Long, R. B. Roncoli, T. H. Sweetser, Trans-Lunar Cruise Trajectory Design of GRAIL (Gravity Recovery and Interior Laboratory) Mission, in: AIAA/AAS Astrodynamics Specialist Conference, AIAA 2010-8384, Toronto, Ontario, Canada, 2010, pp. 2–5.

[30] J. Elliot, L. Alkalai, Lunette: A Network of Lunar Landers for In-Situ Geophysical Science, Acta Astronautica 68 (2011) 1201–1207. doi:10.1016/j.actaastro.2010.10.024.

[31] A. Schuster, R. Jehn, Influence of the Mercury gravity field on the orbit insertion strategy of BepiColombo, Aerospace Science and Technology 39 (2014) 546–551. doi:10.1016/j.ast.2014.06.003.

[32] A. Carbone, M. Cinelli, C. Circi, E. Ortore, Observing Mercury by a quasi-propellantless mission, Celestial Mechanics and Dynamical Astronomy 132 (2020) 1–14. doi:10.1007/s10569-020-9950-0.

[33] N. Hyeraci, F. Topputo, Method to Design Ballistic Capture in the Elliptic Restricted Three-Body Problem, Journal of Guidance, Control, and Dynamics 33 (2010) 1814–1823. doi:10.2514/1.49263.

[34] B. A. Archinal, et al., Report of the IAU Working Group on Cartographic Coordinates and Rotational Elements: 2009, Celestial Mechanics and Dynamical Astronomy 109 (2011) 101–135. doi:10.1007/s10569-010-9320-4.

[35] J. J. Bertin, Hypersonic Aerothermodynamics, AIAA, Washington, DC, 1994.

[36] W. M. Folkner, J. G. Williams, D. H. Boggs, R. S. Park, P. Kuchynka, The Planetary and Lunar Ephemerides DE430 and DE431, Technical Report, IPN Progress Report 42-196, 2014.

[37] C. Circi, P. Teofilatto, Effect of Planetary Eccentricity on Ballistic Capture in the Solar System, Celestial Mechanics and Dynamical Astronomy 93 (2005) 69–86. doi:10.1007/s10569-005-3640-9.

[38] Z.-F. Luo, F. Topputo, Capability of Satellite-aided Ballistic Capture, Communications in Nonlinear Science and Numerical Simulation 48 (2017) 211–223. doi:10.1016/j.cnsns.2016.12.021.

[39] K. Hibbard, L. Glaze, J. Prince, Aerobraking at Venus: A science and technology enabler, Acta Astronautica 73 (2012) 137–143.

[40] A. E. Roy, Orbital Motion, CRC Press, Boca Raton, 2004.

[41] N. Hyeraci, F. Topputo, The Role of True Anomaly in Ballistic Capture, Celestial Mechanics and Dynamical Astronomy 116 (2013) 175–193. doi:10.1007/s10569-013-9481-z.

[42] C. H. Zhou, L. Liu, Time Needed to Use Aerobraking to Insert Planetary Low Orbiters, Journal of Spacecraft TT&C Technology 32 (2013) 438–443. (in Chinese).